Scaling unsteady load alleviation in airfoils with flexible trailing-edges

Shūji Ōtomo (大友衆示),[1,2] Anna M. Young,[3] Edward D. McCarthy,[4] and Ignazio Maria Viola[2,*]

[1]*Department of Mechanical Systems Engineering, Tokyo University of Agriculture and Technology, Koganei 184-8588, Tokyo, Japan*

[2]*School of Engineering, Institute for Energy Systems, University of Edinburgh, Edinburgh EH9 3FB, Scotland, United Kingdom*

[3]*Department of Engineering, University of Bath, Bath BA2 7AY, England, United Kingdom*

[4]*School of Engineering, Institute for Materials and Processes, University of Edinburgh, Edinburgh EH9 3FB, Scotland, United Kingdom*

(Received 16 April 2025; accepted 26 September 2025; published 24 November 2025)

Unsteady load alleviation is crucial for engineering applications such as tidal turbines. Herein, we present an experimental study into the load alleviation capacities of constant-section airfoils with flexible trailing-edges. The trailing-edge studied here consists of two independent flexible skins, enabling large skin deformations and enhanced load alleviation compared to conventional flexible trailing-edge designs. We test high-amplitude plunging kinematics (up to peak-to-peak amplitude of one chord length) at reduced frequency $k = 0.2$ and Reynolds numbers $\mathrm{Re} = \mathcal{O}(10^4)$. To quantify the role of airfoil flexibility, we introduce two Cauchy numbers (Ca_u and Ca_v), which normalize the freestream and plunging velocities, respectively. We demonstrate that both the trailing-edge deflection and the resulting lift alleviation scale with these Cauchy numbers provide a fundamental framework for understanding flexible airfoil dynamics. Furthermore, we propose semi-empirical models for unsteady lift alleviation, which agree with our measurements. These findings lay the groundwork for fully predictive low-order models, advancing the design of passively morphing airfoils for efficient load control in unsteady flow environments.

DOI: 10.1103/6t5l-spq1

I. INTRODUCTION

Unsteady loads drive the design and performance of a wide range of technologies. For example, predicting unsteady forces is critical for controlling small aerial vehicles such as drones [1], whose low inertia compared to large air carriers makes them subject to large accelerations in response to turbulent fluctuations [2–4]. Fatigue loads also drive the design of large structures such as high-rise buildings [5], aircraft wings [6], and wind [7–9] and tidal [10] turbine blades.

The latter application has motivated the present work, in which a morphing blade concept is considered for the mitigation of fatigue loads caused by the unsteady flow characteristics of the tidal current [11]. Unsteadiness in the flow arises from wave-induced current [12], yaw, shear, and turbulence [13].

*Contact author: i.m.viola@ed.ac.uk

Theoretical studies have shown that morphing blades can almost cancel load fluctuations without compromising the mean load [14]. In the aforementioned studies [11,14], two morphing technologies are suggested; one is passively pitching blades, and the other is the flexible trailing-edge blade.

For a passively pitching blade, Ōtomo *et al.* [15] developed a theoretical framework for optimal pitching axis placement to alleviate loads during rapid freestream velocity changes. Liu *et al.* [16] numerically confirmed similar results, showing the optimal axis is about one chord upstream when the freestream velocity increases. Dai *et al.* [17] numerically demonstrated that a turbine with passively pitching blades reduces thrust and torque fluctuations, which was later experimentally verified by Gambuzza *et al.* [18,19].

For airfoils with passive trailing-edge flaps, the experimental and theoretical work by Arredondo-Galeana *et al.* [20] shows that the maximum achievable unsteady load alleviation is proportional to the ratio of the flap length over the chord length. Cordes *et al.* [21] proposed the combined use of passive leading- and trailing-edge flaps, which are connected to each other so that the large pressure difference at the leading-edge drives the angular displacement of the trailing-edge, resulting in a large camber deformation. This measure achieved 60% reduction in the lift fluctuation.

Airfoils with flexible trailing-edges are another technology to mitigate unsteady loads acting on the tidal turbine. This technology is suitable for rapid gust response due to the low inertia of the moving parts. Experiments on extruded rubber blade sections demonstrated the potential for unsteady load mitigation [22]. To achieve the best unsteady load mitigation, however, large deformations are needed, and these may result in buckling of the compressed face of the blade. To avoid issues with buckling, Maguire *et al.* [23] proposed an extruded fibreglass blade section, where the flexible blade skins are both connected to a rigid leading-edge but disconnected at the trailing-edge, resulting in an airfoil with an open trailing-edge. This concept has recently been modeled on a model-scale 1.2 m diameter turbine, where substantial surge load alleviation is projected. Although this technology seems feasible, the underpinning flow-structure interaction has not been established. The present paper aims to investigate the fluid mechanics underlying the unsteady load reduction observed in these recent studies on airfoils with an open flexible trailing edge [23].

The fluid mechanics of flexible airfoils/wings have been studied extensively in the context of bioinspired aerial/water vehicle applications [24]. In particular, passively morphing wings/airfoils that enhance lift [25–28] or propulsive performance [29–32] have been investigated. Cleaver *et al.* [33] undertook an experimental investigation into the effects of a flexible trailing-edge on the thrust generation of plunging airfoils, revealing that the flexible trailing-edge can enhance thrust by 28%. Similarly, Dewey *et al.* [30] confirmed the improved propulsive performance of flexible wings compared with rigid ones. They found scaling laws for thrust production and power input, highlighting that in the flexible regime, the dominant forces are characteristic elastic forces, whereas in the rigid limit, characteristic fluid forces prevail. Later, Quinn *et al.* [29] examined how varying the wings' flexibility and oscillation frequencies affected thrust production and propulsive efficiency. The study found that wings operating near their resonant frequencies exhibited enhanced thrust and efficiency, with performance scaling predictably based on effective flexibility. A linear inviscid model for a passively flexible swimmer was developed by Floryan and Rowley [31]. The study focused on metrics such as trailing edge deflection, thrust coefficient, power coefficient, and efficiency. Fernandez-Feria and Alaminos-Quesada [32] present analytical formulations to analyze the effects of flexibility on the propulsive performance of airfoils with passive chordwise deflection undergoing prescribed pitching and plunging motions.

In fluid-structure interactions involving flexible bodies, the dimensionless Cauchy number Ca, which represents the ratio of hydrodynamic forces to elastic forces, has been used to characterize the coupling between fluid and structural dynamics. Gosselin *et al.* [34] demonstrated through wind tunnel experiments that Cauchy numbers collapse drag for flexible plates undergoing reconfiguration. Kang *et al.* [35] extended the Cauchy number scaling approach to flapping wings and derived empirical scaling laws linking Ca and wing-tip deformation to time-averaged thrust, power input, and propulsive efficiency, with optimal performance occurring near resonant flapping. Luhar

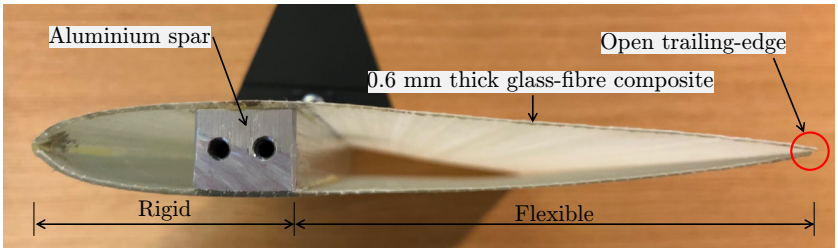

FIG. 1. Airfoil with a flexible and open trailing-edge.

and Nepf [36] applied the Cauchy number to a flexible plate mounted on a wall in wave-induced oscillatory flows, identifying two distinct deformation regimes — quasi-steady and small-excursion — each governed by different power-law scalings of effective plate length with Ca. Jin *et al.* [37] used the Cauchy number to classify flow-induced motions of inclined flexible plates and uncovered transitions between fluttering, twisting, and orbital modes, with distinct force scaling behaviors and mode-dependent drag reductions. However, the scaling laws of passively deforming airfoils have yet to be explored in the context of load alleviation.

Our research aims to bridge this knowledge gap by investigating the fluid mechanics of dynamic load alleviation in highly deformable flexible airfoils. To this end, we experimentally investigate the unsteady load alleviation of an airfoil with a flexible and open trailing-edge. To simulate periodic gusts, the airfoil is subjected to a periodic plunging motion. We introduce two Cauchy numbers — one based on the freestream velocity and the other on the plunging velocity — to represent the mechanisms governing trailing-edge deflection and unsteady load alleviation, and develop semi-empirical models to predict them. This study quantifies the load alleviation performance of the flexible trailing-edge airfoil and establishes scaling laws for its deflection and unsteady loading based on nondimensional flexibility.

The rest of the paper is as follows. Sec. II provides the details of the experiments: experimental setup and airfoil kinematics (Sec. II A), force measurement (Sec. II B), and deformation measurement (Sec. II C). Sec. III presents the results of the experiment and scaling laws: lift and deflection of the steady (Sec. III A) and plunging (Sec. III B) airfoils. Finally, the conclusions are drawn and future research directions are suggested in Sec. IV.

II. EXPERIMENTAL DETAILS

A. Experimental setup and airfoil kinematics

Experiments were performed at the water channel facility of the University of Edinburgh. The test section has dimensions of 0.4 m × 0.38 m × 2 m in width, height, and length, respectively. The turbulence intensity measured by a Laser Doppler Anemometer and a Vectrino Acoustic Doppler Velocimeter was $I_u = 2.8$–6% over the freestream velocity range tested in this work [38–40]. A rigid and a flexible airfoil were tested, both of which were NACA 0012 sections with a chord length of $c = 150$ mm and a span of $s = 300$ mm.

The rigid wing is made of two 3D-printed pieces, which are connected by stainless steel pins. The flexible wing is made of glass fiber skins glued to an aluminum spar at maximum thickness. The skins are not joined at the trailing edge, which allows a large deflection without buckling (Fig. 1). Figure 1 shows the wing model with flexible and open trailing-edge. The leading-edge is nominally rigid as it is strengthened by glass fibre/epoxy plies with the fiber direction aligned with the span of the blade, to maximize strength and stiffness in this direction. The flexible part of the airfoil is made of glass-fibre composite, which has Young's (tensile) modulus $E = 1.86$ GPa and density $\rho_m = 2600$ kg m^{-3}. The length of the flexible skin-section is 2/3 that of the chord ($\ell/c = 2/3$). The trailing-edge surfaces have thickness $b = 0.6$ mm, giving a second moment of area of

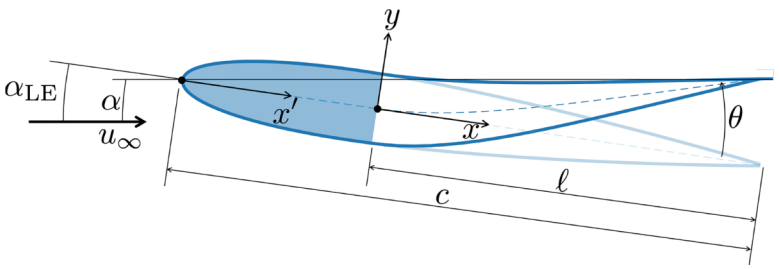

FIG. 2. Geometric definitions of the airfoil with flexible trailing-edge.

$I = sb^3/12 = 5.4 \times 10^{-12}$ m^4. More detailed descriptions of the flexible wing design and manufacturing process are reported in Maguire *et al.* [23].The geometric definitions for this airfoil are shown in Fig. 2. The angle of attack α is defined as the angle made by the freestream u_∞ and the line connecting the leading-edge and trailing-edge. The leading-edge angle of attack α_{LE} is defined as the angle made by the freestream and the leading-edge (rigid part). For the rigid airfoil, these two angles are the same $\alpha = \alpha_{\mathrm{LE}}$.

The experimental setup is illustrated in Fig. 3. Two end-plates were fitted in the water tunnel with 5 mm gaps from the wing tips to minimize three-dimensional effects while allowing the flexible trailing-edge to deflect without contacting the walls. The gap between the end-plates and the channel walls was approximately 0.05 m. Five different freestream velocities $u_\infty \in [0.1, 0.2, 0.3, 0.4, 0.5]$ m s^{-1} were tested to vary the streamwise Cauchy number, which is a

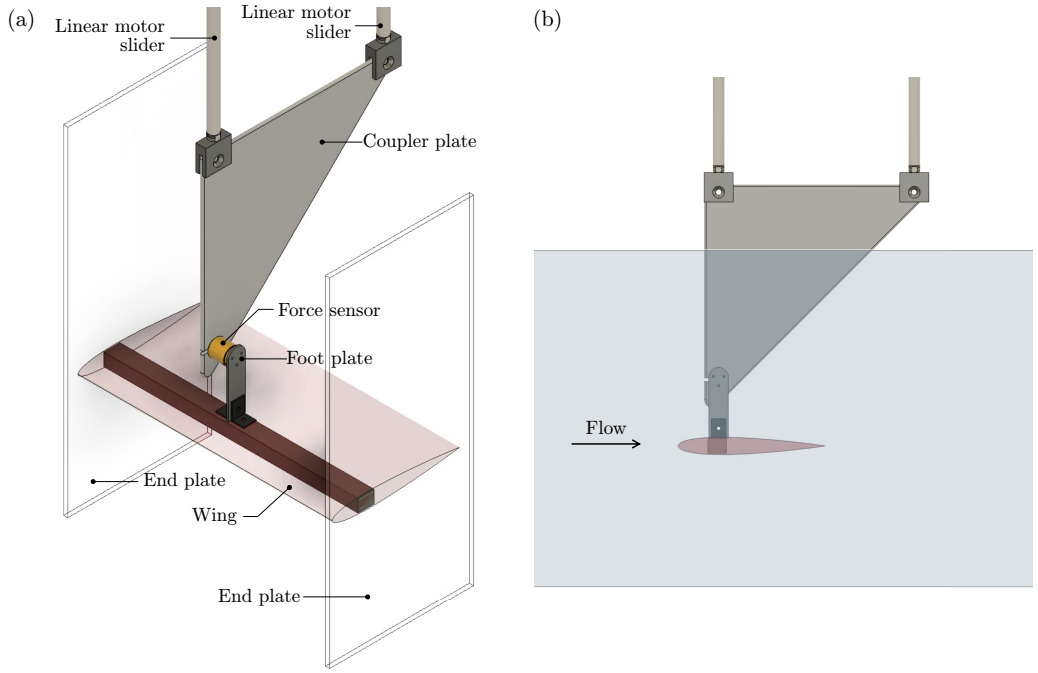

FIG. 3. Schematic of the experimental plunging airfoil test rig: (a) detailed view and (b) side view.

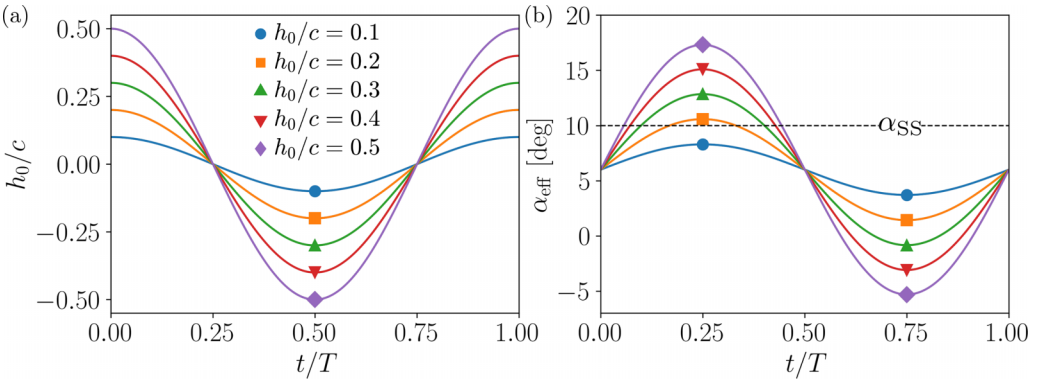

FIG. 4. Kinematics of the plunging motion: time history of (a) airfoil positions and (b) effective angle of attack over a plunging period. The horizontal dashed line in (b) indicates the static stall angle $\alpha_{\text{SS}} = 10^\circ$.

nondimensional flexibility

$$\text{Ca}_u = \frac{\frac{1}{2}\rho_f u_\infty^2 \ell^3 s}{EI}, \tag{1}$$

where ρ_f is the density of water. This maintains the chord-based Reynolds numbers at the same order $\mathcal{O}(10^4)$ ($\text{Re} \in [1.5, 3.0, 4.5, 6.0, 7.5] \times 10^4$) while varying the Cauchy number $\text{Ca}_u \in [0.26, 1.0, 2.2, 4.1, 6.5]$ by more than one order of magnitude, as it is proportional to the velocity squared. As shown later in Sec. III A, hydrodynamic forces are nearly independent of the Reynolds number in this range.

The wing was connected to two linear motors (PS01-23x80F-HP-R20, LinMot) that have ± 0.05 mm position repeatability. The same plunging rig was used in [20,41–43]. To simulate oscillations in the angle of attack, the wing was subjected to a sinusoidal plunging motion, $h/h_0 = \cos(2\pi f t)$ as shown in Fig. 4(a). Here h is the vertical position of the airfoil, h_0 is the plunging amplitude, f is the plunging frequency, and t is time. The leading-edge angle of attack was fixed at $\alpha_{\text{LE}} = 6^\circ$. This angle of attack was chosen because it is representative of the angle of attack for a tidal turbine blade operating at its design point. For example, the mean angle of attack at 75% span was 6° for the turbine used in [14], while Scarlett and Viola [13] and Arredondo-Galeana *et al.* [20] tested 2D airfoil sections at $\alpha = 5^\circ$. The effective angle of attack was $\alpha_{\text{eff}} = \alpha_{\text{LE}} - \arctan(\dot{h}/u_\infty)$ as shown in Fig. 4(b). Five different plunging amplitudes were tested, $h_0/c \in [0.1, 0.2, 0.3, 0.4, 0.5]$, which corresponds to the maximum dimensionless plunging velocities of $\dot{h}_{\text{max}}/u_\infty \in [0.04, 0.08, 0.12, 0.16, 0.20]$. For amplitudes $h_0/c \geqslant 0.3$, the effective angle of attack largely exceeded the static stall angle of NACA 0012 ($\alpha_{\text{SS}} = 10^\circ$) in the Reynolds number range tested in our experiments [marked as a dashed line on Fig. 4(b)]. The reduced frequency was fixed at $k = \pi f c/u_\infty = 0.2$. The tidal turbine blade can experience A reduced frequency range $0 < k < 0.6$ depending on the freestream velocity, tip-speed ratio, and gusts as reported by Sequeira and Miller [44], Scarlett and Viola [13], and Pisetta *et al.* [14]. Our choice of the reduced frequency ($k = 0.2$) and oscillation amplitude ($0.04 \leqslant \dot{h}_{max}/u_\infty \leqslant 0.2$) can be generated, for example, by pressure gusts resulting from waves and turbine rotation through the shear-layer [44].

Here, we introduce the Cauchy number due to the plunging motion,

$$\text{Ca}_v = \frac{\frac{1}{2}\rho_f \dot{h}_{\text{max}}^2 \ell^3 s}{EI}, \tag{2}$$

where $\dot{h}_{\text{max}}$ is the maximum plunging velocity. The kinematics described above mean that a wide range of Ca_v was tested ($2.4 \times 10^{-4} \leqslant \text{Ca}_v \leqslant 1.5 \times 10^{-1}$). Figure 5 shows the variation of Ca_u and Ca_v tested in the experiments.

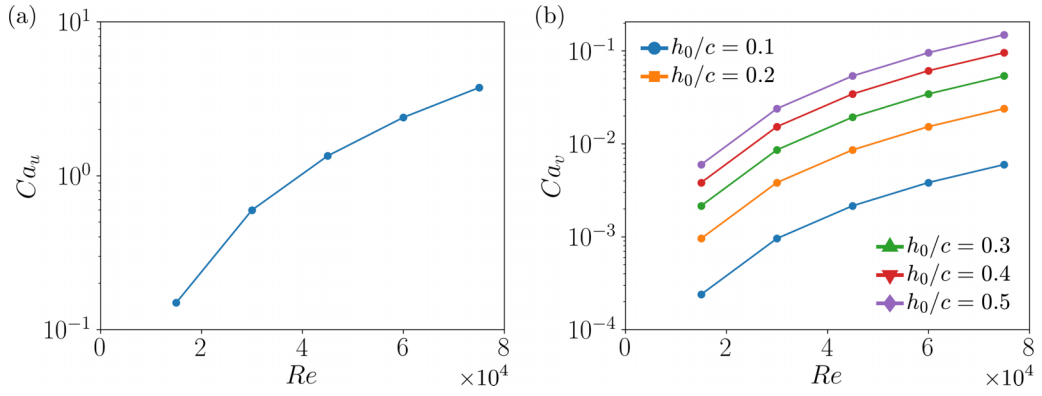

FIG. 5. The range of the two Cauchy numbers and of the Reynolds number tested in the experiment: (a) Ca_u and (b) Ca_v.

B. Force measurement

Forces were recorded at 1000 Hz by a 6-axis force sensor (NANO 17, ATI Industries) with a range ± 25 N and a resolution 0.00625 N, which corresponds to force coefficients of 4 and 0.028 with freestream velocity of 0.5 m s^{-1} and 0.1 m s^{-1}, respectively. Phase-averaging was applied over 50 plunging periods. The recorded force signals were filtered in three steps as suggested by multiple investigators [45–49]. The first filter was a Butterworth low-pass filter with a cut-off frequency of 35 Hz. Then the moving average of 31 points (0.031 s) was applied. Finally, a 4th-order Chebyshev low-pass filter was applied with a cut-off frequency of $12f$ [Hz] and a stop band of 20 dB. In order to separate the inertial forces due to the plunging motion from the hydrodynamic lift and drag forces, the force measurement was performed in quiescent air, and this "no-flow" value was subtracted from the experimental data. Although the trailing-edge deformation is different between tests in water and air, the rigid aluminium spar and the rigid part of the airfoil comprise more than 90% of the airfoil mass, so the effect of trailing-edge deformation on the inertial forces was deemed negligible.

The dynamic load alleviation due to the trailing-edge deflection is evaluated by

$$\varepsilon = \frac{\Delta C_{L,\mathrm{flex}}}{\Delta C_{L,\mathrm{rigid}}}, \tag{3}$$

where $\Delta C_L = C_{L,\max} - C_{L,\min}$ is the peak-to-peak amplitude of the lift coefficient over a plunging cycle. A load alleviation factor of $\varepsilon = 0$ would indicate that the load is completely canceled.

C. Deformation measurements

A CMOS camera was used to optically measure the deformation of the flexible trailing edge, with 120 instantaneous images captured over a plunging cycle. For the deflection measurements, single-shot images were used for analysis (i.e., phase-averaging was not applied). To measure the deformation, the images were processed using the Image Processing Toolbox of Matlab as follows. Figure 6 shows an example of these image processes. Starting from the raw image [Fig 6(a)], the following steps are applied using built-in MATLAB functions:

(1) Image binarisation by Otsu's method with an image intensity threshold of 0.012 (imbinarize function) [Fig. 6(b)].

(2) Remove all connected components that have fewer than 80 pixels for noise reduction (bwareaopen function) [Fig. 6(c)].

(3) Close the gap of the open trailing-edge by detecting a flat morphological structuring element (strel function) [Fig. 6(d)].

(4) Fill the enclosed region using the flood fill algorithm (imfill function) [Fig. 6(e)].

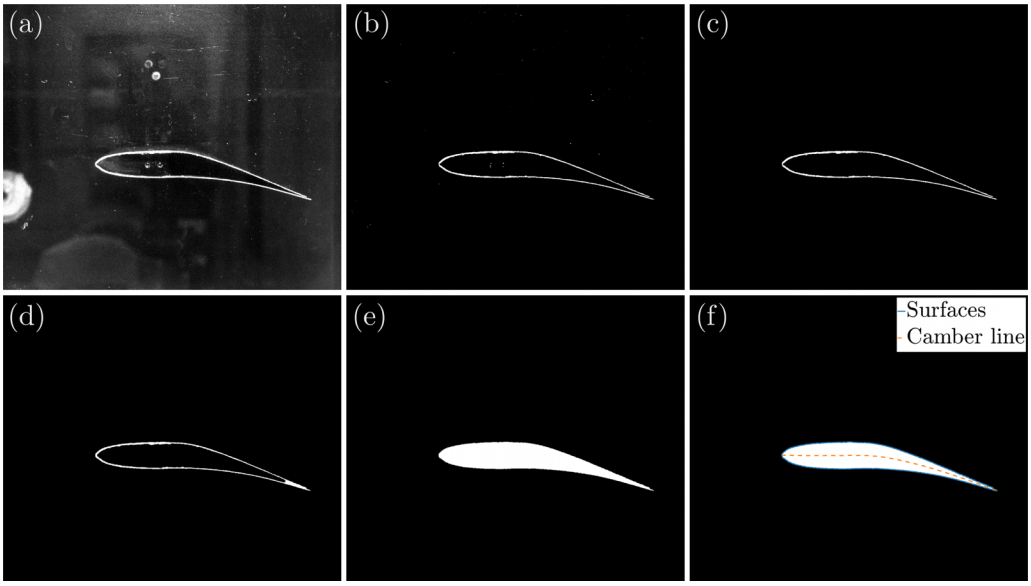

FIG. 6. Surface detection technique: (a) original image (here the contrast is enhanced for the visualization purpose), (b) image binarization, (c) noise removal, (d) fill the gap at the trailing-edge, (e) fill the region enclosed by the wing surfaces, and (f) detect the wing surfaces.

(5) Detect the wing surface by the Moore-Neighbour tracing algorithm (bwboundaries function) [Fig. 6(f)].

Assuming that the pressure variation along the trailing-edge is approximately linear, the detected camber line $\eta(x')$ is fitted to a fifth-order polynomial, which is the solution of Euler-Bernoulli beam theory for the deflection curve of a cantilever beam under a linearly varying load distribution [red dotted line on Fig. 6(f)]. As examples of the force and deflection measurements, Figs. 7(a) and 7(b), respectively, show the time history of the lift coefficient C_L for both rigid and flexible trailing-edge, and trailing-edge deflection θ for $u_\infty = 0.5$ m s^{-1}, $h_0/c = 0.5$ ($Re = 75000$, $\mathrm{Ca}_u = 3.7$, $\mathrm{Ca}_v = 0.15$). Both lift and trailing-edge deflection are sinusoidal. As shown in the figures, we define both ΔC_L and $\Delta\theta$ as peak-to-peak amplitude.

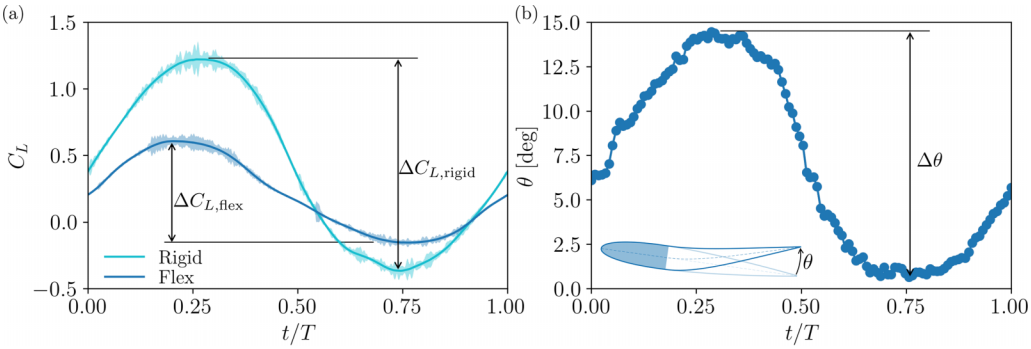

FIG. 7. (a) Time history of lift coefficients of the rigid $C_{L,\mathrm{rigid}}$ and flexible airfoils $C_{L,\mathrm{flex}}$ and (b) time history of the trailing-edge deflection for $u_\infty = 0.5$ m s^{-1}, $h_0/c = 0.5$($Re = 75\,000$, $\mathrm{Ca}_u = 3.7$, $\mathrm{Ca}_v = 0.15$). The shaded regions in (a) show the 95% confidence intervals.

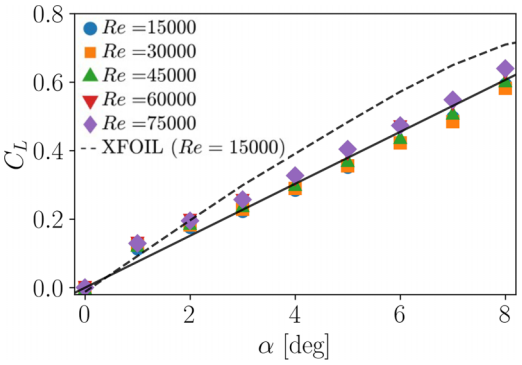

FIG. 8. Steady lift coefficient of the rigid airfoil. The solid black line shows the linear fitted curve, yielding the lift slope of $a_{\text{rigid}} = 4.23°$.

III. RESULTS

A. Steady flow

The steady-state lift coefficients (C_L) for the rigid airfoil are plotted in Fig. 8. The lift calculated from an XFOIL simulation [50] is also compared to the measured values. In XFOIL, we set $N_{\text{crit}} = 0.01$. From the relationship between N_{crit} and turbulence intensity [51], $N_{\text{crit}} = -8.43 - 2.4 \log I_u$, this N_{crit} corresponds to a turbulence intensity of approximately 3%. This is within the range measured in the water tunnel [Sec. II A].

The turbulence transition location on the airfoil was not specified in XFOIL since the separation and transition locations were not measured. Nonetheless, we set $N_{\text{crit}} = 0.01$, which resulted in the transition to occur almost at the leading-edge, at $X/c \approx 0.005$.

The discrepancy between the measured data and XFOIL simulation could be due to the finite height of the water relative to the wing, which is not taken into account in XFOIL [52]. In addition, it is possible that the three-dimensional effects were not completely suppressed because of the gap between the wing tip and the side walls, and this will have led to a smaller lift slope due to the reduction in loading on the outer sections of the wing.

The solid line is the linear best-fit curve $C_L = a_{\text{rigid}}\alpha$ with the lift slope $a_{\text{rigid}} = 4.23$. The result shows that the effect of Reynolds numbers on both lift and drag is negligibly small. The steady lift coefficients (C_L) for the airfoil with the flexible trailing-edge are plotted in Fig. 9. Lift coefficients are respectively plotted against α_{LE} in Fig. 9(a), and against $\alpha - \alpha_{L=0}$ in Fig. 9(b).

For a cambered airfoil, the theoretical lift curve follows

$$C_L = a_{\text{flex}}(\alpha - \alpha_{L=0}). \tag{4}$$

Here $\alpha_{L=0}$ is the zero-lift angle due to the effect of the camber line distribution $\eta(x')$ [53,54],

$$\alpha_{L=0} = -\frac{1}{\pi}\int_0^{\pi} \frac{\mathrm{d}\eta}{\mathrm{d}x'}(\cos\phi - 1)\mathrm{d}\phi. \tag{5}$$

Here ϕ is Glauert's angle $x' = c(1 - \cos\phi)/2$. Since the trailing-edge is flexible, its camber changes with the angle of attack α_{LE} and freestream velocity (Re and Ca_u), which is why C_L varies significantly with Re or Ca_u when plotted against α_{LE} in Fig. 9(a). Instead, if we plot C_L against $\alpha - \alpha_{L=0}$, we see the data collapses more clearly onto a single line as shown in Fig. 9(b). In Fig. 9(b), the solid line is the lift slope ($a_{\text{flex}} = 2.92$) obtained by fitting to the measured data for $0° < \alpha - \alpha_{L=0} < 20°$. The corresponding XFOIL results are shown as hollow markers in Figs. 9(a) and 9(b), showing agreement when Ca_u (and Re) is high, or when the angle of attack ($\alpha - \alpha_{L=0}$) is small. In XFOIL, the optically measured airfoil shape is used (see Section II C).

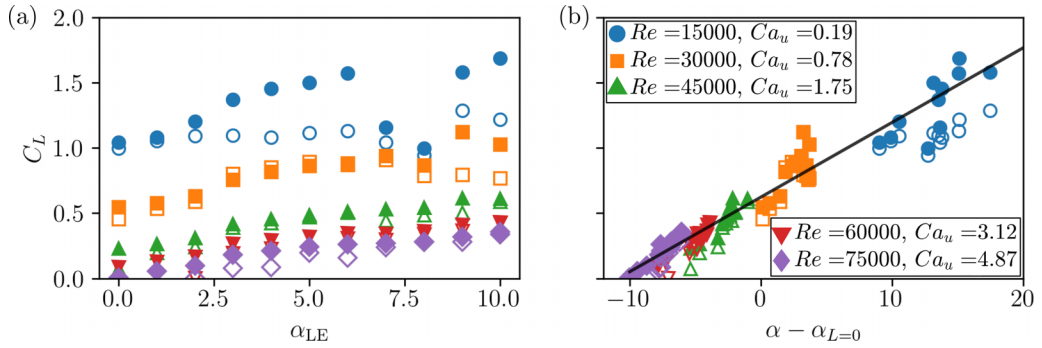

FIG. 9. Steady lift coefficient of the flexible airfoil, (a) plotted against α_{LE}, and (b) plotted against $\alpha - \alpha_{L=0}$. The black solid line in (b) is the lift slope ($a_{\mathrm{flex}} = 2.92^\circ$) obtained by fitting to the measured data for $0^\circ < \alpha - \alpha_{L=0} < 20^\circ$. Hollow markers in (a) and (b) are the results of XFOIL simulation using the measured angle of attack and camber line.

The lift decreases with increasing Ca_u because the trailing-edge deflects downwards due to gravity when Ca_u is low, i.e., when the pressure-side pressure is not high enough to push the skin upward. Therefore, this results in higher angles of attack ($\alpha - \alpha_{L=0}$) for lower Ca_u as shown in Fig. 10, comparing between $\mathrm{Ca}_u = 0.19$ and $\mathrm{Ca}_u = 4.87$. At higher freestream velocity, the trailing-edge becomes squeezed as shown in Fig. 10(b).

B. Trailing-edge deflection and lift alleviation in plunging kinematics

We first look at the forces on the rigid airfoil. Figure 11(a) illustrates the amplitude of the lift coefficient for the rigid airfoil. The lift amplitude increases approximately linearly with the plunging amplitude h_0/c, agreeing with the prediction of unsteady lift based on thin-airfoil theory [54,55]

$$C_{L,\mathrm{rigid}} = -\frac{\pi c}{2u_\infty^2}\ddot{h} + a_{\mathrm{rigid}}\left(\alpha - \frac{\dot{h}}{u_\infty}\right), \tag{6}$$

where the first and second terms represent added mass and circulatory forces, respectively. Here we use the experimentally measured $a_{\mathrm{rigid}} = 4.23$ (c.f. Fig. 8) instead of 2π. Equation 6 is the same as Theodorsen's theory [56], with Theodorsen's function being $C(k) = 1$, which is the value at $k = 0$. Here we take $C(k) = 1$, following the approach of Baik *et al.* [46] who found Theodorsen's theory with $C(k) = 1$ successfully captures the lift coefficient when the effective angles of attack are high. Figure 11(b) compares lift between the experiments and theory for $h_0/c = 0.1$ and $h_0/c = 0.5$,

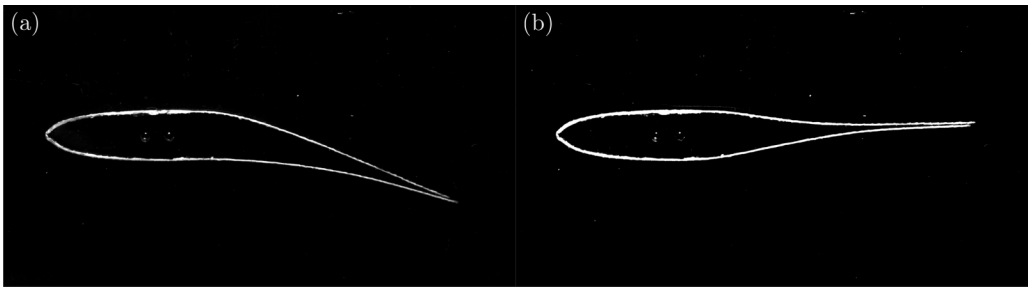

FIG. 10. Comparison of trailing-edge deflection for the steady flow case at $\alpha_{\mathrm{LE}} = 0^\circ$ between (a) $\mathrm{Re} = 15000$, $\mathrm{Ca}_u = 0.19$ and (b) $\mathrm{Re} = 75000$, $\mathrm{Ca}_u = 4.87$.

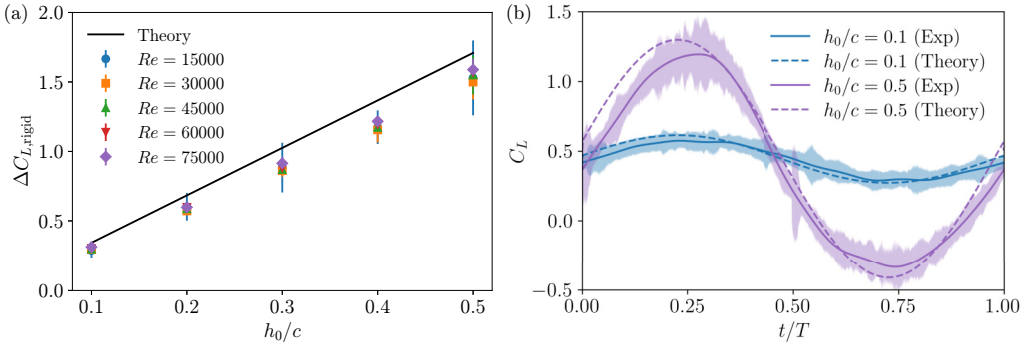

FIG. 11. (a) The amplitude of lift coefficient ΔC_L for the rigid airfoil undergoing plunging motion, compared between experiments and theory (Eq. (6) and (b) the time history of lift coefficient for $h_0/c = 0.1$ and $h_0/c = 0.5$ compared between experiment and theory (Eq. (6). The shaded regions show the 95% confidence intervals.

respectively. The predicted lift is in good agreement with the measured values, even at the largest amplitude tested in this work ($h_0/c = 0.5$), where the instantaneous angle of attack exceeds the static stall angle for a large part of the cycle (c.f. Fig 4), and so some departure from the linear model is expected. Figure 12 shows the mean trailing-edge deflection $\overline{\theta}$ and mean lift coefficient $\overline{C_L}$ for the flexible foil under each plunging motion. The data are plotted against Ca_u and compared with that of the steady case at $\alpha_{\mathrm{LE}} = 6^\circ$. It can be seen that the mean values depend on Ca_u, and are not influenced by the plunging motion (i.e., h_0/c or Ca_v). In addition, the mean values are comparable to those of the steady flow case. The mean trailing-edge deflection $\overline{\theta}$ for the steady case at $\mathrm{Ca}_u = 2.2$ is smaller than that for the plunging cases. We interpret this as a non-physical result caused by measurement errors in the instantaneous deflection measurement, since the lift coefficient $\overline{C_L}$ for the steady case at $\mathrm{Ca}_u = 2.2$ aligns with that of the plunging case.

This collapse in mean deflection $\overline{\theta}$ and lift $\overline{C_L}$ shows that the trailing edge deflection, and hence lift, is dependent on the dimensionless group associated with flexibility, the Cauchy number Ca_u, and not on the plunging amplitude. Figure 13 depicts the deflection amplitudes over each plunging cycle. In Fig. 13(a), the deflection amplitude normalized by the maximum induced angle of attack $\Delta\theta/(\dot{h}_{\max}/u_\infty)$ is plotted against Ca_u. The fitted curve is $\Delta\theta/(\dot{h}_{\max}/u_\infty) = a_1 \mathrm{Ca}_u^{1/4}$ with a constant $a_1 = 0.82$ is found by the least-squares method. We leave the reasoning as to why the normalized deflection is proportional to $\mathrm{Ca}_u^{1/4}$ for future studies. Since $\Delta\theta/(\dot{h}_{\max}/u_\infty) \propto \mathrm{Ca}_u^{1/4}$, $\mathrm{Ca}_u \propto u_\infty^2$

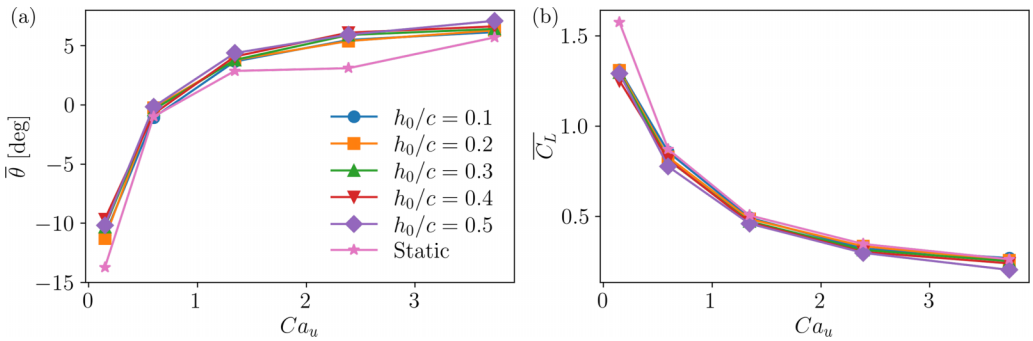

FIG. 12. (a) Time-averaged trailing-edge deflection $\overline{\theta}$ and (b) time-averaged lift coefficient $\overline{C_L}$ scaled by Ca_u for different plunging amplitudes.

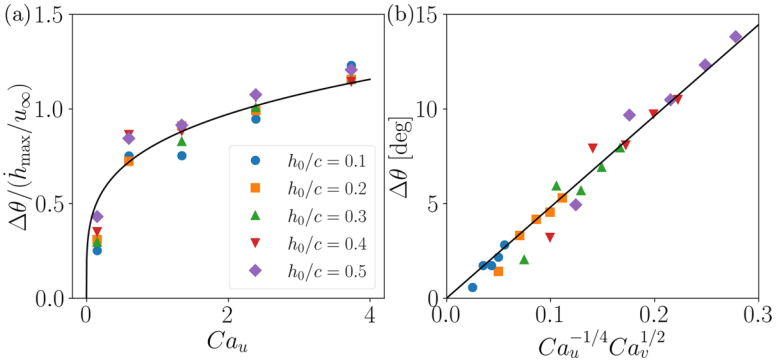

FIG. 13. Scaled trailing-edge deflection amplitude $\Delta\theta$: (a) deflection amplitude normalized by the maximum induced angle of attack by the plunging motion $\Delta\theta/(\dot{h}_{\max}/u_\infty)$ versus Ca_u. The solid line is the best-fit curve $(\Delta\theta/(\dot{h}_{\max}/u_\infty) = a_1\mathrm{Ca}_u^{1/4}$ with a_1 as a fitting parameter), and (b) the deflection amplitude $\Delta\theta$ versus $\mathrm{Ca}_u^{-1/4}\mathrm{Ca}_v^{1/2}$. The solid line is the linear regression line.

(Eq. (1), and $\mathrm{Ca}_v \propto \dot{h}_{\max}^2$ (Eq. (2), the deflection amplitude $\Delta\theta$ should follow $\Delta\theta \propto \mathrm{Ca}_u^{-1/4}\mathrm{Ca}_v^{1/2}$. This is shown in Fig. 13(b), in which the data collapse onto the linear regression line.

The lift coefficient amplitudes of the flexible airfoil normalized by the induced angles of attack $\Delta C_{L,\mathrm{flex}}/(\dot{h}_{\max}/u_\infty)$ are plotted against two different parameters in Fig. 14. In Fig. 14(a), $\Delta C_{L,\mathrm{flex}}/(\dot{h}_{\max}/u_\infty)$ is plotted against Ca_u. The normalized lift amplitude decreases with increasing Ca_u, but also depends on the plunging amplitude h_0/c. When taking $\mathrm{Ca}_u\mathrm{Ca}_v$ as the horizontal axis, all the data collapse onto a single curve as shown in Fig. 14(b). This curve is found to be $\Delta C_{L,\mathrm{flex}}/(\dot{h}_{\max}/u_\infty) = (\mathrm{Ca}_u\mathrm{Ca}_v)^{-1/4} + a_2$ with a_2 being a constant and hence the lift amplitude is expressed as

$$\Delta C_{L,\mathrm{flex}} = (\mathrm{Ca}_u\mathrm{Ca}_v)^{-1/4}\frac{\dot{h}_{\max}}{u_\infty} + a_2\frac{\dot{h}_{\max}}{u_\infty}. \tag{7}$$

For a flexible airfoil, we can rewrite the circulatory part of the linear theory (Eq. (6) as

$$C_{L,\mathrm{flex}}^{\mathrm{Circ}}(t) = a_{\mathrm{flex}}\left(\alpha_{\mathrm{LE}} + \alpha_{\mathrm{morph}}(t) - \frac{\dot{h}(t)}{u_\infty}\right). \tag{8}$$

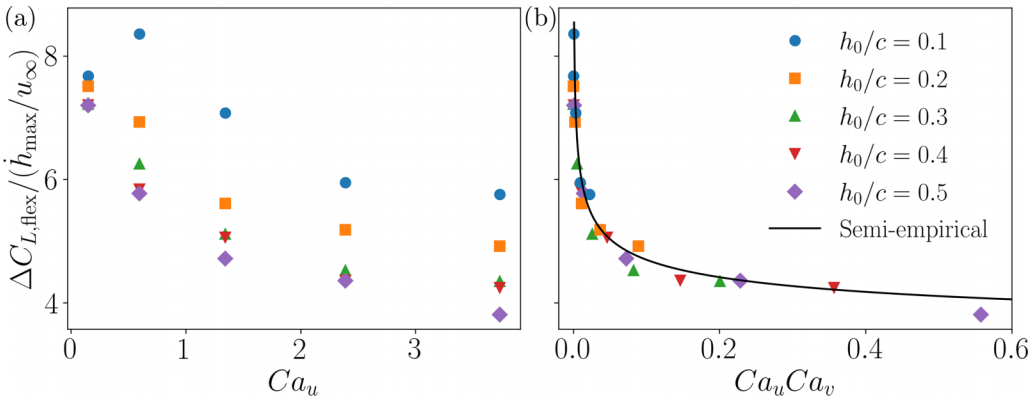

FIG. 14. Scaled lift coefficient amplitude of the flexible airfoil $\Delta C_{L,\mathrm{flex}}/(\dot{h}_{\max}/u_\infty)$ plotted against (a) Ca_u, (b) $\mathrm{Ca}_u\mathrm{Ca}_v$.

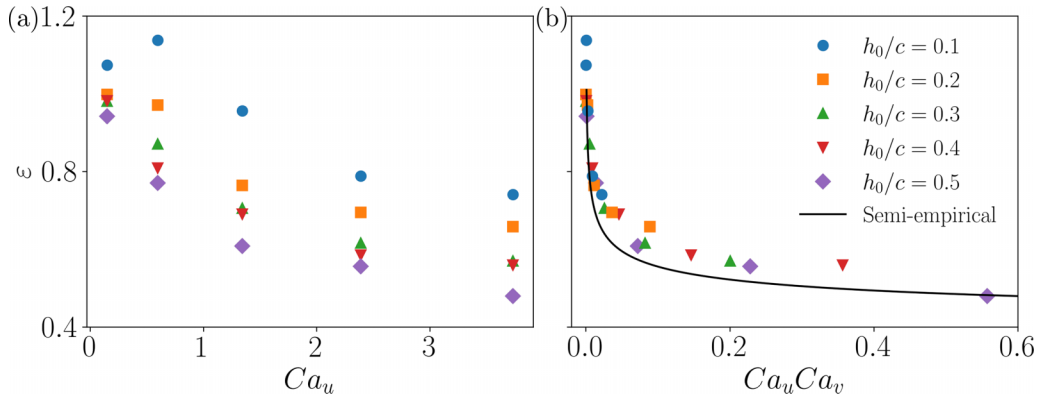

FIG. 15. Dynamic lift alleviation ε plotted against (a) Ca_u and (b) $\mathrm{Ca}_u\mathrm{Ca}_v$.

The first term on the right-hand side is the mean term that is not affected by the plunging motion, as we see in Fig. 12. The second term $\alpha_{\mathrm{morph}}(t)$ is the change in the angle of attack due to the flexible trailing-edge, which also includes the change in the camber. The third term is the contribution from the plunging motion, due to the change in the plunging-induced angle of attack $\dot{h}/u_\infty$. Comparing the two equations above (Eqs. 7 and 8), the second term on the right-hand side of Eq. (7) represents the contribution from the plunging motion, and hence the fitting parameter a_2 is the lift slope of the flexible airfoil. In fact, if we take $a_2 = a_{\mathrm{flex}} = 2.92$ as shown in the solid line in Fig. 14(b), the agreement with the measured values is remarkable.

The first term on the right-hand side of Eq. (7), $(\mathrm{Ca}_u\mathrm{Ca}_v)^{-1/4}\dot{h}_{\mathrm{max}}/u_\infty$, is related to the change in the angle of attack and camber due to the passive morphing, but we leave the theoretical explanation for future studies.

Figure 15(a) shows the result of the dynamic lift alleviation ε against Ca_u. The dynamic lift has a dependency on both the Cauchy number Ca_u and the plunging amplitude h_0/c. A lift alleviation of approximately 52% is achieved at $\mathrm{Ca}_u = 3.7$ for the maximum plunging amplitude tested ($h_0/c = 0.5$).From the circulatory lift from linear theory for rigid airfoils (Eq. (6), the peak-to-peak lift amplitude is

$$\Delta C_{L,\mathrm{rigid}} = 2a_{\mathrm{rigid}}\frac{\dot{h}_{\mathrm{max}}}{u_\infty}. \tag{9}$$

Thus, from Eq. (7) with $a_2 = a_{\mathrm{flex}}$ and Eq. (9), the lift alleviation ε should follow

$$\varepsilon = \frac{\Delta C_{L,\mathrm{flex}}}{\Delta C_{L,\mathrm{rigid}}} = \frac{1}{2a_{\mathrm{rigid}}}[(\mathrm{Ca}_u\mathrm{Ca}_v)^{-1/4} + a_{\mathrm{flex}}]. \tag{10}$$

This is plotted as a solid line in Fig. 15(b), showing a reasonable agreement with the measured dynamic lift alleviation ε, which collapses when plotted against $(\mathrm{Ca}_u\mathrm{Ca}_v)^{1/4}$. The semi-empirical model slightly underpredicts $\varepsilon = \Delta C_{L,\mathrm{flex}}/\Delta C_{L,\mathrm{rigid}}$ because $\Delta C_{L,\mathrm{rigid}}$ is slightly overpredicted by thin-airfoil theory [Eq. (6) and Fig. 11(a)]. From Eq. (10), in the limit of $\mathrm{Ca}_u\mathrm{Ca}_v \to \infty$ (i.e., the trailing-edge has perfect flexibility), the asymptotic value takes $\varepsilon_{\mathrm{Ca}_u\mathrm{Ca}_v\to\infty} = a_{\mathrm{flex}}/(2a_{\mathrm{rigid}}) = 0.345$ with $a_{\mathrm{rigid}} = 4.23$ and $a_{\mathrm{flex}} = 2.92$. In the quasi-steady model developed by Arredondo-Galeana *et al.* [20], the load alleviation for an airfoil with a passive trailing-edge flap is equal to the ratio of the flap length over the chord length: $\varepsilon = 1 - \ell/c$. For our airfoil with $\ell/c = 2/3$, this is $\varepsilon_{\mathrm{Ca}_u\mathrm{Ca}_v\to\infty} = 1 - \ell/c = 0.333$, which is close to our formulation. This means that the lift slope in our formulation α_{flex} implicitly includes the effect of the length of the flexible trailing-edge, i.e., the longer the flexible trailing-edge, the smaller the lift slope.

IV. CONCLUSIONS

An experimental investigation has been undertaken into the unsteady load mitigation of sinusoidally plunging, constant-section airfoils with flexible and open trailing-edges at the Reynolds number $\mathrm{Re} = \mathcal{O}(10^4)$ and reduced frequency $k = 0.2$. The open trailing-edge design allows a large deformation (over 15°) and hence a large load alleviation (up to ∼50%). Two different nondimensional parameters for plunging kinematics have been defined, which govern the flexibility: Cauchy numbers (Ca_u and Ca_v) based on the freestream velocity and the plunging velocity, respectively. For the present work, the ranges tested are $0.26 \leqslant \mathrm{Ca}_u \leqslant 6.5$ and $2.4 \times 10^{-4} \leqslant \mathrm{Ca}_v \leqslant 1.5 \times 10^{-1}$.

A load alleviation of approximately 52% was observed at the highest Cauchy numbers. Scaling laws have been identified both for the deflection and the load of airfoils with flexible trailing-edges. The trailing-edge deformation amplitude $\Delta\theta$ has been found to be proportional to $\mathrm{Ca}_u^{-1/4}\mathrm{Ca}_v^{1/2}$. The normalized lift amplitudes of the flexible airfoil $\Delta C_{L,\mathrm{flex}}/(\dot{h}_{\max}/u_\infty)$ collapse with the product of the two Cauchy numbers, $\mathrm{Ca}_u\mathrm{Ca}_v$, and are proportional to $(\mathrm{Ca}_u\mathrm{Ca}_v)^{-1/4}$. The proportional constant was found to be the lift slope of the flexible airfoil; this has been explained by analysis of the quasi-steady circulatory lift model for flexible airfoils. It has been further shown that the dynamic lift alleviation, $\varepsilon = \Delta C_{L,\mathrm{flex}}/\Delta C_{L,\mathrm{rigid}}$, is proportional to $(\mathrm{Ca}_u\mathrm{Ca}_v)^{-1/4}$. Again, the result is consistent with thin-airfoil theory.

We expect the scaling laws to apply to other airfoil geometries as the material stiffness EI is the only necessary structural parameter. Future studies should be performed to see if the scaling laws are applicable to different kinematics (pitching, combined pitching and plunging, or canonical gust flows). For pitching airfoils, the velocity induced by the pitch motion can be represented at the three-quarter chord, based on unsteady thin-airfoil theory. Therefore, the induced velocity can be decomposed into streamwise and stream-normal directions, which can be included in Ca_u and Ca_v, respectively.

We deem the scaling law presented in this paper may need to be corrected for massively separated flows where the effect of coherent vortices, such as leading-edge and trailing-edge vortices, is significant. In other words, this occurs when Ca_v is comparable in magnitude to Ca_u. For example, Martinez-Muriel *et al.* [57] reported that their quasi-steady lift model fails when a coherent leading-edge vortex is formed and interacts with the passively deflecting trailing-edge flap, as it advects downstream. Future studies can be conducted for such aggressive kinematics and include the effect of coherent vortices by estimating the induced velocities due to coherent vortices.

ACKNOWLEDGMENTS

This research is supported by Engineering and Physical Sciences Research Council grant, Morphing-Blades: New-Concept Turbine Blades for Unsteady Load Mitigation (Grant No. EP/V009443/1) and JSPS KAKENHI (Grant No. JP24K17204). The authors would like to express their gratitude to Doug Halley for his assistance in the construction of the experimental apparatus.

DATA AVAILABILITY

The data that support the findings of this article are openly available [58].

[1] D. Floreano and R. J. Wood, Science, technology and the future of small autonomous drones, Nature (London) **521**, 460 (2015).

[2] T. J. Mueller and J. D. DeLaurier, Aerodynamics of small vehicles, Annu. Rev. Fluid Mech. **35**, 89 (2003).

[3] A. R. Jones, O. Cetiner, and M. J. Smith, Physics and modeling of large flow disturbances: Discrete gust encounters for modern air vehicles, Annu. Rev. Fluid Mech. **54**, 469 (2022).

[4] D. Greenblatt and D. R. Williams, Flow control for unmanned air vehicles, Annu. Rev. Fluid Mech. **54**, 383 (2022).
[5] J. Cermak, Aerodynamics of buildings, Annu. Rev. Fluid Mech. **8**, 75 (1976).
[6] W. J. McCroskey, Unsteady airfoils, Annu. Rev. Fluid Mech. **14**, 285 (1982).
[7] J. N. Sørensen, Aerodynamic aspects of wind energy conversion, Annu. Rev. Fluid Mech. **43**, 427 (2011).
[8] R. J. Stevens and C. Meneveau, Flow structure and turbulence in wind farms, Annu. Rev. Fluid Mech. **49**, 311 (2017).
[9] C. R. Shapiro, G. M. Starke, and D. F. Gayme, Turbulence and control of wind farms, Annu. Rev. Control. Robotics Auton. Syst. **5**, 579 (2022).
[10] T. A. Adcock, S. Draper, R. H. Willden, and C. R. Vogel, The fluid mechanics of tidal stream energy conversion, Annu. Rev. Fluid Mech. **53**, 287 (2021).
[11] I. M. Viola, G. Pisetta, W. Dai, A. Arredondo-Galeana, A. Young, and A. Smyth, Morphing blades: Theory and proof of principles, Int. Mar. Energy J. **5**, 183 (2022).
[12] G. T. Scarlett, B. Sellar, T. van den Bremer, and I. M. Viola, Unsteady hydrodynamics of a full-scale tidal turbine operating in large wave conditions, Renew. Energy **143**, 199 (2019).
[13] G. T. Scarlett and I. M. Viola, Unsteady hydrodynamics of tidal turbine blades, Renew. Energy **146**, 843 (2020).
[14] G. Pisetta, R. Le Mestre, and I. M. Viola, Morphing blades for tidal turbines: A theoretical study, Renew. Energy **183**, 802 (2022).
[15] S. Ōtomo, S. Gambuzza, Y. Liu, A. M. Young, R. Broglia, E. D. McCarthy, and I. M. Viola, A general framework for the design of efficient passive pitch systems, Phys. Fluids **36**, 067122 (2024).
[16] Y. Liu, R. Broglia, A. M. Young, E. D. McCarthy, and I. M. Viola, Unsteady load mitigation through passive pitch, J. Fluids Struct. **131**, 104216 (2024).
[17] W. Dai, R. Broglia, and I. M. Viola, Mitigation of rotor thrust fluctuations through passive pitch, J. Fluids Struct. **112**, 103599 (2022).
[18] S. Gambuzza, G. Pisetta, T. Davey, J. Steynor, and I. M. Viola, Model-scale experiments of passive pitch control for tidal turbines, Renew. Energy **205**, 10 (2023).
[19] S. Gambuzza, P. Sunil, M. Felli, A. M. Young, R. Broglia, E. D. McCarthy, and I. M. Viola, Power and thrust control by passive pitch for tidal turbines, Renew. Energy **239**, 121921 (2025).
[20] A. Arredondo-Galeana, A. M. Young, A. S. Smyth, and I. M. Viola, Unsteady load mitigation through a passive trailing-edge flap, J. Fluids Struct. **106**, 103352 (2021).
[21] U. Cordes, B. Lambie, K. Hufnagel, H. Spiegelberg, G. Kampers, and C. Tropea, The adaptive camber concept - a passive approach for gust load alleviation on wind turbines, Wind Energy **21**, 732 (2018).
[22] S. Tully and I. M. Viola, Reducing the wave-induced loading of tidal turbine blades through the use of a flexible blade, in *16th International Symposium on Transport Phenomena and Dynamics of Rotating Machinery* (Hawaii, Honolulu, 2016), p. 9.
[23] J. M. Maguire, D. Mamalis, S. Ōtomo, and E. D. McCarthy, Passively morphing trailing edge design for composite tidal turbine blades, Compos. Struct. **337**, 118090 (2024).
[24] H. Liu, S. Wang, and T. Liu, Vortices and forces in biological flight: Insects, birds, and bats, Annu. Rev. Fluid Mech. **56**, 147 (2024).
[25] I. Gursul, D. Cleaver, and Z. Wang, Control of low Reynolds number flows by means of fluid–structure interactions, Prog. Aerosp. Sci. **64**, 17 (2014).
[26] A. Gehrke, J. Richeux, E. Uksul, and K. Mulleners, Aeroelastic characterisation of a bio-inspired flapping membrane wing, Bioinspir. Biomim. **17**, 065004 (2022).
[27] S. Ochi, S. Kai, K. Takase, K. Soneda, T. Imamura, K. Rinoie, and T. Yokozeki, Aeroelastic simulation and experimental validation of a 3D-printed passive morphing airfoil, AIAA J. 1 (2024).
[28] A. Gehrke and K. Mulleners, Highly deformable flapping membrane wings suppress the leading edge vortex in hover to perform better, Proc. Natl. Acad. Sci. USA **122**, e2410833121 (2025).
[29] D. B. Quinn, G. V. Lauder, and A. J. Smits, Scaling the propulsive performance of heaving flexible panels, J. Fluid Mech. **738**, 250 (2014).

[30] P. A. Dewey, B. M. Boschitsch, K. W. Moored, H. A. Stone, and A. J. Smits, Scaling laws for the thrust production of flexible pitching panels, J. Fluid Mech. **732**, 29 (2013).
[31] D. Floryan and C. W. Rowley, Clarifying the relationship between efficiency and resonance for flexible inertial swimmers, J. Fluid Mech. **853**, 271 (2018).
[32] R. Fernandez-Feria and J. Alaminos-Quesada, Analytical results for the propulsion performance of a flexible foil with prescribed pitching and heaving motions and passive small deflection, J. Fluid Mech. **910**, A43 (2021).
[33] D. Cleaver, I. Gursul, D. Calderon, and Z. Wang, Thrust enhancement due to flexible trailing-edge of plunging foils, J. Fluids Struct. **51**, 401 (2014).
[34] F. Gosselin, E. De Langre, and B. A. Machado-Almeida, Drag reduction of flexible plates by reconfiguration, J. Fluid Mech. **650**, 319 (2010).
[35] C.-K. Kang, H. Aono, C. E. Cesnik, and W. Shyy, Effects of flexibility on the aerodynamic performance of flapping wings, J. Fluid Mech. **689**, 32 (2011).
[36] M. Luhar and H. Nepf, Wave-induced dynamics of flexible blades, J. Fluids Struct. **61**, 20 (2016).
[37] Y. Jin, J.-T. Kim, S. Fu, and L. P. Chamorro, Flow-induced motions of flexible plates: Fluttering, twisting and orbital modes, J. Fluid Mech. **864**, 273 (2019).
[38] R. E. Muir, A. Arredondo-Galeana, and I. M. Viola, The leading-edge vortex of swift wing-shaped delta wings, R. Soc. Open Sci. **4**, 170077 (2017).
[39] J.-B. R. Souppez, P. Bot, and I. M. Viola, Turbulent flow around circular arcs, Phys. Fluids **34**, 015121 (2022).
[40] J.-B. R. Souppez and I. M. Viola, Water tunnel testing of downwind yacht sails, Exp. Fluids **65**, 15 (2024).
[41] H. J. Bird, S. Otomo, K. K. Ramesh, and I. M. Viola, A geometrically non-linear time-domain unsteady lifting-line theory, in *Proceedings of the AIAA Scitech 2019 Forum* (San Diego, California, 2019).
[42] H. J. Bird, K. K. Ramesh, S. Otomo, and I. M. Viola, Leading edge vortex formation on finite wings using vortex particles, in *Proceedings of the AIAA SciTech Forum* (AIAA, Reston, 2021), pp. 19–21.
[43] H. J. Bird, K. Ramesh, S. Ōtomo, and I. Maria Viola, Usefulness of inviscid linear unsteady lifting-line theory for viscous large-amplitude problems, AIAA J. **60**, 598 (2022).
[44] C. L. Sequeira and R. J. Miller, Unsteady gust response of tidal stream turbines, *2014 Oceans-St. John's* (IEEE, Piscataway, NJ, 2014), pp. 1–10.
[45] K. O. Granlund, M. V. Ol, and L. P. Bernal, Unsteady pitching flat plates, J. Fluid Mech. **733**, R5 (2013).
[46] Y. S. Baik, L. P. Bernal, K. Granlund, and M. V. Ol, Unsteady force generation and vortex dynamics of pitching and plunging aerofoils, J. Fluid Mech. **709**, 37 (2012).
[47] K. Ramesh, A. Gopalarathnam, J. R. Edwards, M. V. Ol, and K. Granlund, An unsteady airfoil theory applied to pitching motions validated against experiment and computation, Theor. Comput. Fluid Dyn. **27**, 843 (2013).
[48] R. T. Jantzen, K. Taira, K. O. Granlund, and M. V. Ol, Vortex dynamics around pitching plates, Phys. Fluids **26**, 053606 (2014).
[49] S. Ōtomo, S. Henne, K. Mulleners, K. Ramesh, and I. M. Viola, Unsteady lift on a high-amplitude pitching aerofoil, Exp. Fluids **62**, 1 (2021).
[50] M. Drela, Xfoil: An analysis and design system for low Reynolds number airfoils, in *Low Reynolds number aerodynamics*, edited by T. J. Mueller (Springer, Heidelberg, 1989), Vol. 54, pp. 1–12.
[51] L. M. Mack, Transition and laminar instability, Technical Report No. JPL-PUBL-77-15 (Jet Propulsion Laboratory, California Institute of Technology, 1977), https://ntrs.nasa.gov/citations/19770017114?utm_source=chatgpt.com.
[52] T. F. Brooks, D. S. Pope, and M. A. Marcolini, Airfoil self-noise and prediction, Technical Report No. L-16528 (1989).
[53] J. Anderson, *Fundamentals of Aerodynamics (SI units)*, 5th ed. (McGraw Hill, New York, 2011).
[54] J. Katz and A. Plotkin, *Low-Speed Aerodynamics* (Cambridge University Press, Cambridge, 2001), Vol. 13.
[55] G. J. Leishman, *Principles of Helicopter Aerodynamics* (Cambridge University Press, Cambridge, 2006).

[56] T. Theodorsen, General theory of aerodynamic instability and the mechanism of flutter, Report No. NACA-TR-496 (1934).
[57] C. Martinez-Muriel, I. M. Viola, M. Garcia-Villalba, and O. Flores, Mitigating unsteady loads at low Reynolds numbers using a passive trailing-edge flap, J. Fluids Structures **138**, 104392 (2025).
[58] S. Ōtomo, A. Young, E. McCarthy, and I. M. Viola, Dataset for lift and trailing-edge deflection of passively morphing aerofoils (2025) https://datashare.ed.ac.uk/handle/10283/8981.